applied sciences

MDPI

Article

On the Link between Diesel Spray Asymmetry and Off-Axis Needle Displacement

Giancarlo Chiatti †, Ornella Chiavola †, Pierluigi Frezzolini † and Fulvio Palmieri *,†

Dipartimento di Ingegneria, Università degli Studi Roma TRE, 00146 Rome, Italy;
giancarlo.chiatti@uniroma3.it (G.C.); ornella.chiavola@uniroma3.it (O.C.); p.frezzolini@gmail.com (P.F.)
* Correspondence: fulvio.palmieri@uniroma3.it; Tel.: +39-0657-333-493
† All authors contributed equally to the work.

Academic Editor: Jose Ramon Serrano
Received: 31 January 2017; Accepted: 31 March 2017; Published: 11 April 2017

Abstract: Cutting edge experiments and thorough investigations have pointed out that radial components affect the needle lift of diesel nozzles. So far, the effects of such needle "off-axis" have been investigated within the nozzle and immediately downstream from the hole outlet. Here, the focus has been extended to the spray ambient, far outside a multi-hole VCO (Valve Covered Orifice) nozzle. A reference off-axis configuration of the needle has been defined and used to investigate its effects on the spray, in terms of hole-to-hole differences. Indeed, the spray alterations due to the needle position have been addressed for those factors, such as the velocity-coefficient C_V and the area-coefficient C_A, able to describe the nozzle flow behavior under needle off-axis. The investigation has been based on 3D-CFD (three-dimensional computational fluid dynamics) campaigns. The modeling of diesel nozzle flow has been interfaced to the Eulerian–Eulerian near-nozzle spray simulation, initializing the break-up model on the basis of the transient flow conditions at each hole outlet section. The dense spray simulation has been on-line coupled to the Eulerian–Lagrangian modeling of the dilute spray region. Quantitative results on each fuel spray have been provided (in terms of penetration and Sauter Mean Diameter). The range of variability within the spray characteristics are expected to vary has been found and reported, providing reference information for lumped parameter models and other related investigations.

Keywords: diesel spray; needle off-axis; hole-to-hole spray differences

1. Introduction

Tracing the evolution of the multi-hole nozzles used in direct injection diesel engines, VCO (Valve Covered Orifice) layout was introduced with the advent of the first generation of common rail injectors, replacing the mini-sac layout. This step allowed the substantial reduction of unburned hydrocarbons emission. In fact, the fuel remaining inside the injector tip is released after the end of injection [1]; very recent studies are better focusing the causes of the so called "injector dribble", whose impact on emission is becoming crucial [2]. The implications of in-nozzle phenomena at the early beginning and after the end of injection have been related to pollutant emission and to deposit formation within the holes. In such a scenario, where low lifts and short injection shots are usual, some recent contributions have concerned the phenomenology of the very early phases of injection [3], of the primary atomization of the liquid [4] and of the phases in which fuel is trapped in the holes and in the sac at the beginning and at the end of injection [5].

Significant efforts have been devoted at comparing sac and VCO nozzles, focusing the attention on the internal nozzle flow, on the rate of injection and on the spray behavior [6–8]. Besides some advantages, the major drawback of the VCO layout is represented by the irregularities of the spray that occur at low needle lift; these abnormalities assume relevance because they are related to the

formation of particulate matter [1]. At the time of the introduction of the VCO layout, this aspect had a relatively little importance, since low needle lift was the only operating condition of pilot injections.

The introduction of multiple-injection technique was complemented by the wide adoption of micro-sac geometries. These geometries resulted in being more suited to the characteristics of the second generation injectors (in the compromise between the reduction of unburned hydrocarbons and particulate matter). Indeed, the multiple-injection strategies have required a significant improvement of the injector dynamics, which was also translated into a substantial reduction of the maximum needle lift. Since the needle was located to work almost always at low lift (ballistic displacement), the micro-sac layout represented a better compromise than the VCO layout in producing regular sprays, with low formation of particulate matter [9] and low release of unburned fuel, in agreement with the emission regulations at that time.

As highlighted by the latest research activities [10], the release level of unburned fuel typical of micro-sac nozzles is no longer tolerable, according to the trend of unburned hydrocarbons emission regulation. From this viewpoint, the VCO design will predictably be reassessed and developed again [11,12], in order to minimize the content of liquid fuel that is trapped when the needle is closed. In the light of this, it is believed that investigations on behavior of VCO nozzles under real operating conditions represent an interesting and significant topic.

The abnormal behavior of the spray produced by the VCO nozzle has been observed by several investigators. The VCO-spray features reported in the literature show differences in the macroscopic characteristics among the fuel jets. The differences relate to the spray penetration and to the spray angle [13,14]. If the presence of significant defects of the nozzle is excluded, this behavior suggests that the fuel flows through each hole in a particular way. After the first experiments carried out on sprays from VCO injectors, investigators had suggested that the spray abnormalities were due to the misalignment of the needle during injection; the misalignment had been considered capable of significantly influencing the fuel flow pattern at the hole inlet section; indeed, in VCO nozzles, the needle remains in the immediate proximity of the inlet section of the holes for the whole injection event [14,15]. The super-accurate design and manufacturing of the nozzles, provided with expensive double guides for the needle in some cases, has been the main technical approach that enabled VCO-injector manufacturers to stabilize the behavior of the spray as much as possible.

Some experimental investigations based on X-ray techniques have confirmed that needle displacement is affected by major radial oscillations [16]. The experiments have later also allowed for detecting the amount of needle movement in the radial direction [17].

In agreement with these findings, further contributions and simulation campaigns were carried out to quantify the influence of the needle misalignment on the distribution of the fuel flow out of each hole. The results reported in the literature have highlighted that the flow field upstream of the holes is directly affected by the needle position during injection. In more detail, the position of the needle determines the flow characteristics at each hole inlet, influencing the downstream fuel flow [18–20].

The current experimental techniques allow for making a very fine analysis both on the needle displacement during injection and the internal multiphase nozzle flow [21]. Equally advanced are the techniques developed for the diagnosis of the spray [22] features.

In principle, the link between the needle alignment and the characteristics of each spray could be simultaneously studied by combining nozzle and spray diagnostics. Unfortunately, research activities that combine the two types of analysis are not yet reported in the literature.

The 3D-CFD (three-dimensional computational fluid dynamics) is the only practical way to consider, step by step in time, the link between what happens inside the nozzle and what happens outside; this work is oriented in this direction, and the aim is to observe in what measures the off-axis position of the needle is reflected by the spray anomalies, quantifying and delimiting the differences that could be expected due to the off-axis movement of the needle; according to the aforementioned motivations, the study considers a VCO layout.

In the first phase of the work, the reference nozzle geometry and the reference injection event have been identified. Subsequently, the 3D-CFD simulation approach has been defined, relying on the modeling of the internal nozzle flow; once characterized, it has been interfaced to the spray simulation, initializing the primary break-up model on the basis of the transient flow conditions at each outlet section of the multi-hole VCO nozzle. Among the possibilities, the spray modeling has been based on a coupled Euler–Lagrangian approach, whose features have recently been reported in the literature [23]. The simulations have been carried out in *FIRE*™ environment [24] (by AVL List GmbH, Graz, Austria). The following section describes the relevant assumptions and the details of the proposed approach. The results section reports the main points of investigation; and the conclusions are discussed in the last paragraph.

2. Materials and Methods

2.1. Reference Nozzle and Off-Axis Configuration of the Needle

The reference VCO layout for the investigation has been identified among the real applications, yet preserving the general validity of the study. The choice fell on a commercial six hole nozzle that equips the second generation electro-injectors (injection pressure up to 1600 bar) in the automotive field (cylinder displacement in the range of 500 cm^3). Once defined, the real nozzle has been sectioned and optically investigated (Figure 1); thus, the internal geometry has been digitalized to allow the construction of the computational grids. The relevant nozzle features are reported in Table 1. The simulations have been extended to a half-sector of the whole geometry, decreasing the computational costs, thanks to the plane-symmetry of the implemented off-axis configuration (as described in the next paragraph).

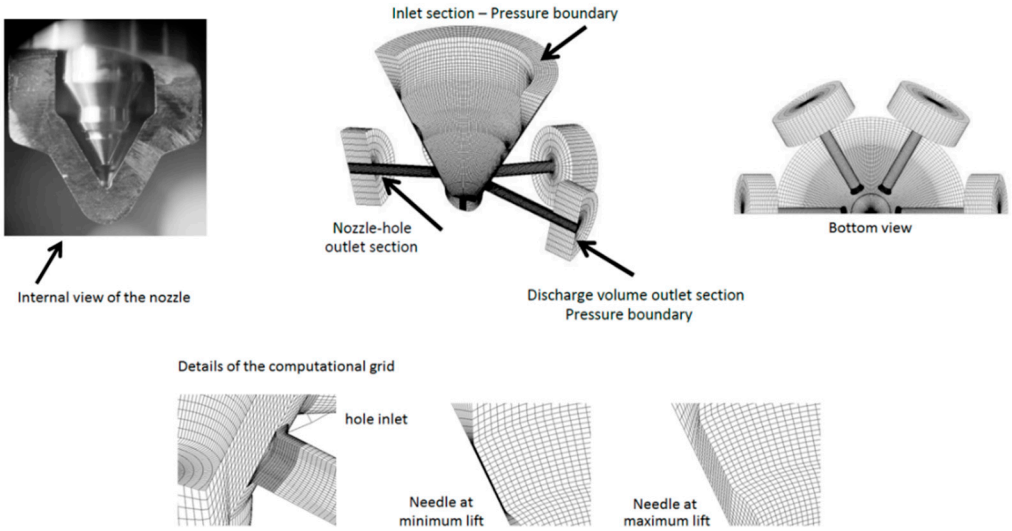

Figure 1. Internal view of the investigated nozzle and computational nozzle grid.

Table 1. Specifications of nozzle layout.

Nozzle Layout	
Nozzle type	VCO [1]
Number of nozzle holes	6
Hole diameter (mm)	0.175
Length to diameter ratio	5.7
Hole plane angle (deg)	156

[1] VCO: Valve Covered Orifice.

The nozzle flow simulation considers the operation of the needle under ballistic conditions; the adopted operating condition of the needle reflects the multiple-injection strategies, where low lifts and short injection shots are usual. The purely axial needle lift law is obtained by means of a lumped-parameter mechanical-hydraulic model of the complete electro-injector. The model has been built in the *LMS Amesim* environment [25] (by Siemens AG Digital Factory, Nurnberg, Germany), and it has been experimentally validated in terms of Rate of Injection (ROI), transient pressure signal at injector inlet and cumulative injected mass. ROI measure is based on the well-known Bosch Tube system [26], in which the pressure wave is measured by means of a piezo-resistive pressure sensor (*4067-type* by Kistler, Winterthur, Switzerland). The same sensor is used to measure the pressure signal at injector inlet, and the cumulative mass of 1000 injection shots has been measured by analytical balance. The complete information about the model and its validation is reported in [27]. The adopted needle lift curve and the related test conditions are reported in Figure 2.

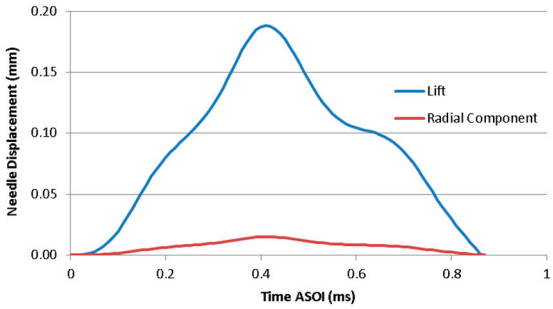

Injection pressure	1400 bar
Injection duration	0.88 ms
Spray chamber pressure	7 bar
Spray chamber temperature	393.15 K
Fuel type	ISO 4113

Figure 2. Needle displacement time traces (**left**); test conditions (**right**).

The grid of the nozzle body is structured and made of hexahedral elements. The hole grids are structured as well, and they are connected to the nozzle body through arbitrary grid interfaces. Such a meshing approach allows for adopting identical grids for the holes. Different meshing approaches are possible, such as the Cartesian cut cell method [17], but the same mesh topology for each hole is not guaranteed. Therefore, the adopted meshing approach is viewed as a good practice in the attempt to avoid hole-to-hole grid dependencies. The modeling of needle displacement in the current CFD analysis is based on "mesh deformation", which consists of the use of a mesh-set to reproduce the needle displacement step-by-step. In such an approach, some cell layers undergo a deformation according to the needle displacement at each simulation time-step and never change in number. To prevent the adoption of extremely small cells at a near-zero needle lift, the approach proposed in [17] has been adopted, so that a minimal gap has been used (4 μm, which correspond to about 2.2% of the maximum lift). It has to be noted that the cell layers in the gap at minimum lift, made of hexahedral elements, have orthogonal faces; during the needle lift, the cells of the layer are deformed, with a well-tolerated skewness level at maximum lift. The nozzle computational grid and the relevant details are visible in Figure 1.

2.2. Off-Axis Displacement of the Needle

As reported in [17], the off-axis displacement is due to needle oscillations during the injection; these have been identified as cantilever-type vibrations of the needle with respect to the needle guide, which is located upstream of the tip. Separate analysis of x and y motion components (assuming the needle is lifting along z) revealed that these lateral oscillations are quite often in-phase. Moreover, it has been evidenced that the oscillation occurs mainly on one side of the nozzle and the needle tip does not move back to the opposite side, crossing the centerline. In [17], the attention is focused on relatively long injections (2 ms), in which a specific needle wobble profile has been considered, with the needle performing three oscillation peaks in the x-plane. Since these lateral oscillations are purely mechanical in nature, the oscillation period is independent from injection duration [28]. In the current

investigation, as the considered injection shot is shorter, the occurrence of just one oscillation peak is assumed. According to [17], it is assumed that the needle performs a pure two-dimensional translation, starting from the closing position; the radial component affecting the needle displacement has been set as a percent (8%) of the maximum vertical displacement (Figure 2, left).

As shown in the scheme of Figure 3, the needle displacement is along a straight direction, represented here by the A-B line. The A-B line and the axes of two opposite holes (*N*1 and *N*4) lie in the same plane. As visible, hole *N*1 is the most approached by the needle, whereas the other *N*4 is in the opposite condition. Thus, in the case of *N*1 and *N*4, the off-axis displacement allows for evaluating the influence of the needle proximity to the hole during the injection. In the case of *N*2 and *N*3, the off-axis displacement alters the proximity and also the symmetry of the needle towards the axes of the holes (*N*2 and *N*3). In summary, the current off-axis needle displacement has been chosen to realize a different configuration between the needle and each of the four holes, as evidenced by Figure 3 (right).

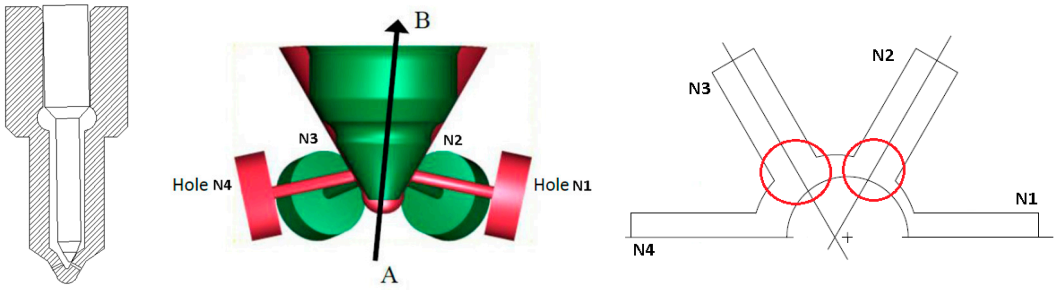

Figure 3. Off-axis needle displacement (cantilever-type) (**left**); adopted scheme for off-axis displacement (translation along A-B line) (**center**); displacement influence on the hole inlets (**right**).

2.3. Modeling Approach

The adopted concept of the coupling among the nozzle flow, the Eulerian and the Lagrangian spray models is shown in Figure 4 (left). The first, independent, simulation step is the transient nozzle flow simulation, taking into account the three-dimensional needle movement and cavitation effects; for certain discrete time steps (360 in the current analysis), the flow data of the bulk liquid and the vapor phase at each orifice outlet are stored on a data file providing the boundary conditions for the dense spray simulation, in agreement with the conclusions reported in [29], where this approach is outlined as appropriate when evaluating the effects of asymmetries in multihole nozzles. The dense spray region is simulated with the Eulerian spray approach, whereas the dilute spray is based on the DDM (Discrete Droplet Method)–Lagrangian approach.

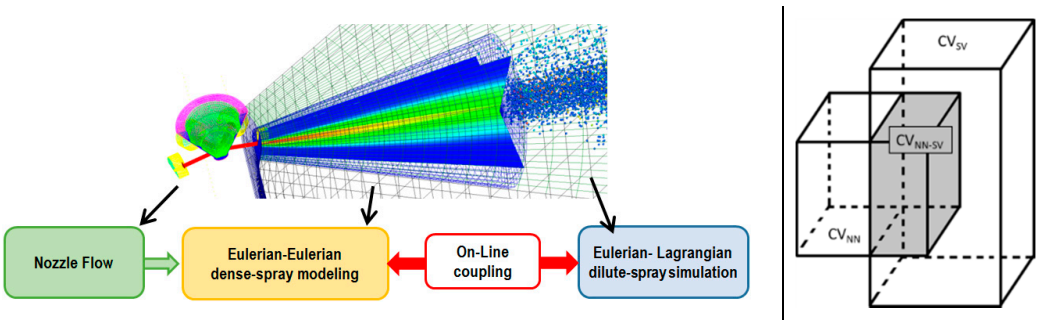

Figure 4. Simulation approach based on coupling among models (**left**); scheme of Control Volume intersection between elements belonging to the Near-Nozzle mesh and to the Spray Volume mesh (**right**).

2.3.1. Coupled Eulerian–Lagrangian Spray Simulation

On the modeling of spray process, the most of the strategies falls into the aforesaid two basic formulations: the Eulerian–Lagrangian (EL) and the Eulerian–Eulerian (EE) methods. Compared to the EL method, the EE method is suitable for calculation of flows with higher droplet concentration [30], whereas the other approach is appropriate in the simulation of the diluted spray region. Here, the EL and EE methods are used in combination. In the light of the contributions reported in the literature, the combination of EE and EL methods is placed in the frame of two coupling approaches; these are the "ELSA model" (Euler Lagrange Spray Atomisation) [31–35] and the "ACCI server" (AVL Coupling Code Interface) [36–39].

In the ELSA methodology, the Eulerian spray is treated as a single-phase flow represented by a liquid-gas mixture. By means of additional transport equations for the liquid mass fraction and the liquid surface density, the spray atomization is modeled; if the spray is dilute enough, Lagrangian spray parcels are initiated.

In the current work, the approach based on the ACCI server is adopted, where the coupling between Eulerian and Lagrangian spray is achieved as follows. The dense spray is calculated with the Eulerian spray approach in a separate simulation client, on a highly resolved computational grid representing the near nozzle region. In the second simulation client (here, the spray-volume ambient), the Lagrangian approach is used for the dilute spray modeling. Indeed, the computational grid of the spray-volume client covers the entire simulation domain, including also the Eulerian spray region. Thus, an overlapping region is defined, in which the simulation is performed on both clients. The interactions between the gaseous and the liquid phases in the Eulerian spray simulation are transferred as source terms to the spray-volume client simulation. The data transfer between the simulation clients is managed via the ACCI server. The coupled simulation starts with the computational initialization of both simulation clients; the fluid properties are determined and the flow field of the Lagrangian client is initialized. The first exchange event taking place is the initialization, when the initial gas flow field of the Eulerian spray client is fully determined by the initial flow field of the Lagrangian client. The three velocity components—pressure, enthalpy, species mass fractions and turbulence transport quantities—are mapped and transferred via the server. The other exchange events are determined by the simulation time steps of the clients. Data exchange from the Lagrangian to the Eulerian spray client is performed to obtain the flow field boundaries of the Eulerian spray simulation; at every exchange event, the 3D flow field of the Lagrangian client is mapped onto the boundary surface of the Eulerian spray client. Data exchange in the other direction occurs due to the interaction between droplets and gas. Drag forces introduce source terms in the momentum conservation equation; mass exchange from evaporation causes sources in the continuity and species transport equations. In the overlapping domain, the gas phase flow field is calculated on both simulation clients. Thus, the source terms from the phase interactions in momentum, mass and energy conservation equations as well as the sources from the species transport equations are transferred from the Eulerian spray to the Lagrangian client. This means that, although there is no liquid phase in the overlapping domain of the Lagrangian client, the gas phase is fully encountered by the interactions with the droplet phases.

The liquid droplets leaving the Eulerian spray client initiate the spray parcels at the Lagrangian client. Conservation of liquid mass, momentum, energy and number of droplets are required criteria for the interface. The algorithm for creating new parcels by fulfilling the conservation criteria is based on the idea that a new parcel is created, if the accumulated liquid mass of a droplet phase exceeds a certain mass threshold. The preparation of new spray parcels is fully calculated by the Eulerian spray client; the interface server sends the parcel initialization data to the Lagrangian client where the new parcels are introduced. A loop over all droplet phases and over all open boundary faces is performed for every time step to check the droplet mass leaving the domain.

Since different meshes are used for the near-nozzle and spray ambient simulations (according to the scheme of Figure 4 (right)), the source terms mapping is performed in a conservative manner using weighting factors. For extensive attributes, such as mass or momentum sources, weighting factors wf_{ex}

are calculated from the intersection volumes between the two client domains, as shown in Equation (1). For example, the mass source term S in a control volume of the spray mesh is calculated from all values in the control volumes in near nozzle mesh, as shown in Equation (2). In the case of intensive attributes such as mass fraction, velocity, pressure or temperature, where attributes do not depend on the size of control volumes, and the weighting factors wf_{in} are defined as shown in Equation(3):

$$wf_{ex} = \frac{CV_{NN-SV}}{CV_{NN}}, \tag{1}$$

$$S_{SV} = \sum_{s} wf_{ex} S_{NN}, \tag{2}$$

$$wf_{in} = \frac{CV_{NN-SV}}{CV_{SV}}. \tag{3}$$

2.3.2. Near Nozzle Eulerian Spray Modeling

The Eulerian spray modeling is based on a multiphase method [40]. The gas and the liquid are treated as interpenetrating continuous phases, characterized by their volume fraction in the control volume. A number n of phases is considered. The first (n = 1) is the gaseous one, and it represents the gas and the fuel vapor in the spray ambient. The other phases (n = 2, ... , $n-1$) represent the droplet size classes, whereas the phase n is the bulk liquid phase preceding the break-up process. For each phase, the set of conservation equations is solved separately. Mass—Equation (4), momentum—Equation (5) and enthalpy—Equation (6) conservation equations for the phase k are reported in the following. On the right hand side of each equation, there are the exchange-terms Γ_{kl}, M_{kl}, H_{kl} (mass, momentum, enthalpy) between the phases k and l; these are the terms that contain the physics of the spray. The left-hand side of each equation is made of two terms, the rate of change and the convective transport of the phase flow property. The volume fraction of each phase must fulfill the compatibility condition, Equation (7):

$$\frac{\partial \alpha_k \rho_k}{\partial t} + \nabla \cdot (\alpha_k \rho_k v_k) = \sum_{l=1,\, l \neq k}^{n} \Gamma_{kl}, \tag{4}$$

$$\frac{\partial \alpha_k \rho_k v_k}{\partial t} + \nabla \cdot (\alpha_k \rho_k v_k v_k) = -\alpha_k \nabla p + \nabla \cdot \alpha_k \left(\tau_k + \tau_k^t\right) + \alpha_k \rho_k f + \sum_{l=1,\, l \neq k}^{n} \mathrm{M}_{kl} + v_k \sum_{l=1,\, l \neq k}^{n} \Gamma_{kl}, \tag{5}$$

$$\frac{\partial \alpha_k \rho_k h_k}{\partial t} + \nabla \cdot (\alpha_k \rho_k v_k h_k) = \nabla \cdot \alpha_k \left(q_k + q_k^t\right) + \alpha_k \rho_k f \cdot v_k + \alpha_k \rho_k \theta_k + \alpha_k \tau_k : \nabla v_k + \alpha_k \frac{dp}{dt} \sum_{l=1,\, l \neq k}^{n} \mathrm{H}_{kl} + h_k \sum_{l=1,\, l \neq k}^{n} \Gamma_{kl}, \tag{6}$$

$$\sum_{k=1}^{n} \alpha_k = 1. \tag{7}$$

The Eulerian spray model is framed in the RANS (Reynolds-averaged Navier-Stokes) approach, with k-epsilon closure. The Eulerian–Eulerian spray model here adopted has been extensively validated against experimental data, as reported in [39], concerning atomization and evaporation process, and in [23] concerning reactive cases.

2.4. Primary Break-Up

2.4.1. Core Injection Approach under Nozzle Flow Local Information

The primary break-up rate in the spray domain considers two independent mechanisms and is determined by the liquid turbulence in the nozzle orifice and by the aerodynamic conditions in the spray region. According to this approach, the turbulent fluctuations in the liquid jet create the initial perturbations on the surface. These grow under the action of aerodynamic pressure forces until they detach as atomized droplets. The coherent liquid core region at the nozzle exit, where primary break-up occurs, is calculated from a mass balance at the volume elements of the liquid core. The liquid core itself is modeled through a blob-injection scheme, in which the blob diameter is constant and the blob number varies according to the mass loss due to primary break-up. The determination

of mass loss from this region is based on the rate-approach $\mathrm{d}R/\mathrm{d}t$, where $\mathrm{d}R/\mathrm{d}t$ is viewed as the artificial-radius change of the assumed blob injection. The rate $\mathrm{d}R/\mathrm{d}t$ is an artificial dimension for the mass loss because the number of blobs decreases while the blob radius stays constant. In the current scheme, such a concept is applied locally, by means of the separate multi-phase nozzle flow simulation (Figure 5, left). For each "j" face of the nozzle orifice, the rate $\mathrm{d}R_\mathrm{j}/\mathrm{d}t$ is calculated from the two-phase nozzle flow simulation; the atomization length scale $L_{\mathrm{A,j}}$ is equal to the turbulent length scale $L_{\mathrm{T,j}}$ as reported in Equation (8). The turbulent length-scale $L_{\mathrm{T,j}}$ and the atomization time scale $\tau_{\mathrm{A,j}}$ are determined locally for each j face. The expression for $L_{\mathrm{T,j}}$ is given by Equation (9), whereas the expression for the local atomization time scale $\tau_{\mathrm{A,j}}$ is given by Equation (10):

$$\frac{\mathrm{d}R_\mathrm{j}}{\mathrm{d}t} = \frac{L_{\mathrm{A,j}}}{\tau_{\mathrm{A,j}}}, \tag{8}$$

$$L_{\mathrm{T,j}} = C_2 C_\mu \frac{k_\mathrm{j}^{1.5}}{\varepsilon_\mathrm{j}}, \tag{9}$$

$$\tau_{\mathrm{A,j}} = C_1 \tau_{\mathrm{T,j}} + C_3 \tau_{\mathrm{W,j}}. \tag{10}$$

The local turbulent time scale $\tau_{\mathrm{T,j}}$ is calculated from Equation (11) and the local aerodynamic time and length scale, $\tau_{\mathrm{W,j}}$ and $L_{\mathrm{W,j}}$, are calculated according to Equation (12):

$$\tau_{\mathrm{T,j}} = C_\mu \frac{k_\mathrm{j}}{\varepsilon_\mathrm{j}}, \tag{11}$$

$$\tau_{\mathrm{W,j}} = \frac{L_{\mathrm{W,j}}}{\sqrt{\frac{\rho_1 \rho_\mathrm{N} |V_\mathrm{N} - V_1|^2}{(\rho_\mathrm{N} + \rho_1)^2} - \frac{\sigma}{(\rho_\mathrm{N} + \rho_1) L_{\mathrm{W,j}}}}} \text{ and } L_{\mathrm{W,j}} = 2 L_{\mathrm{T,j}}. \tag{12}$$

The local diameter of the product droplets resulting from this model is proportional to the turbulent length scale, Equation (13):

$$D_{\mathrm{d,j}} = 2 L_{\mathrm{T,j}}. \tag{13}$$

The adopted model gives different break-up rates $\mathrm{d}R_\mathrm{j}/\mathrm{d}t$ and different product droplet diameter for each face of the nozzle orifice. Each face of the orifice determines the break-up rate on an idealized blob injection surface; therefore, the local rate of change $\mathrm{d}R_\mathrm{j}/\mathrm{d}t$ is mapped onto the corresponding blob surface and represents a certain fraction of the mass loss (Figure 5, right).

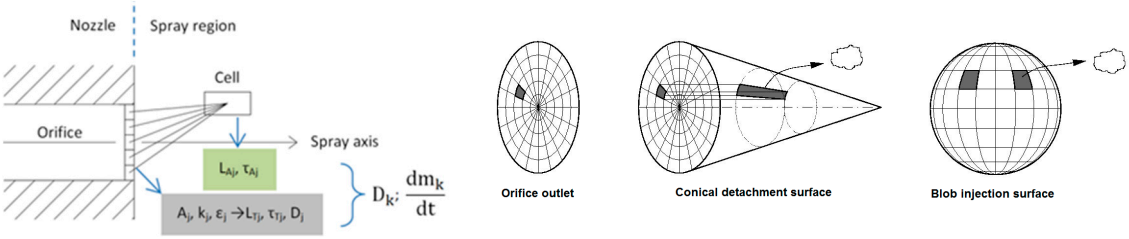

Figure 5. Assignment of orifice cells to primary break-up rate of continuous liquid phase (**left**); local nozzle flow conditions influence on primary break-up rate at the blob (**right**).

The target phase of the liquid droplet phases is determined by the local product droplet diameter $D_{\mathrm{d,j}}$. These droplet diameters are sorted into five different predetermined droplet size classes [39].

The primary break-up mass rate per unit volume from the bulk liquid phase (N-phase) into the droplet phase k, $\Gamma_{\mathrm{P,Nk}}$ is computed according to Equation (14), where α_N is the volume fraction of N-phase, A_{nozz} is the surface area of the entire nozzle orifice and A_i is the local surface area of each face in the nozzle orifice. $\dot{M}_{\mathrm{N,j}}$ denotes the local primary break-up mass transfer rate per blob surface

and is determined by Equation (15). The function δ_k ($D_{d,i}$) results from the sorting process of the local primary break-up rate values, and it is either one or zero. If the local droplet diameter $D_{d,i}$ belongs to size class k, and the function δ_k ($D_{d,i}$) is one; otherwise, it is zero:

$$\Gamma_{P,Nk} = \frac{6\alpha_N}{D_N} \sum_{j=1}^{n_{orifice}} \frac{A_j}{A_{nozz}} \dot{M}_{N,j} \delta_k \left(D_{d,j} \right) = -\Gamma_{P,kN}, \quad (14)$$

$$\dot{M}_{N,j} = \rho_N \frac{dR_j}{dt} = \rho_N \frac{L_{A,j}}{\tau_{A,j}}. \quad (15)$$

2.4.2. Lagrangian Spray Modeling

The injection process in the current investigation has been modeled within a quiescent spray-chamber (7 bar pressure) in non-evaporative conditions (393.15 K). The domain is the same in all simulation cases and it is built on polar symmetry, where the nozzle axis is in the central position. In the near tip region, in all the tested cases, the mesh is built with the same resolution of the nozzle hole, and it gradually widens as the distance from the hole increases. The spray calculation is based on the Discrete Droplet Method (DDM); the k-ε turbulence closure for the RANS-equations solution has been adopted. The WAVE model [41] has been used to simulate the droplet secondary break-up process, assuming that the growth of an initial perturbation on a liquid surface is linked to its wavelength and to other physical and dynamic parameters of the injected fuel and the fluid domain. The particle interaction model based on the statistical approach proposed by O' Rourke [42] has been adopted.

2.5. Multiphase Nozzle Flow Modeling

The internal nozzle flow is simulated through the Eulerian multi-fluid method, Equations (4)–(7). In the current application, the flow is supposed to be isothermal and comprises $n = 3$ phases, namely, the liquid fuel, its vapor and air. The flow model is based on the RANS approach with k–ζ–f turbulence closure model, with a standard wall function. The turbulent stresses in the continuous phases are computed by adding to the standard turbulent viscosity a bubble-induced viscosity term, according to the Sato model [43]. The interfacial exchange terms, relevant for cavitation between liquid and fuel vapor, are represented by the mass- and momentum-exchange terms, which take into account the microscopic effects at the interface between the phases. Concerning the mass exchange term between liquid fuel and vapor, the non-linear form of the Rayleigh–Plesset equation is used to describe bubble growth dynamics. The interfacial momentum exchange (between liquid fuel and vapor) is modeled taking drag and turbulent dispersion effects into account, while neglecting inertia and lift effects. The drag model on the bubbles uses drag coefficient C_D, based on spherical shape and is dependent on Reynolds number. The turbulent mixing process between phases relies on the momentum interaction at the interface, which induces turbulence production on the liquid phase through the Sato model [43]. The state of bubble diameter is a function of position and time (poly-dispersed diameter); coalescence due to turbulent random collisions, breakup (induced by turbulent impact) and bubble generation due to cavitation are the mechanisms taken into account. The complete mathematical description of this approach in the modeling of multiphase nozzle flow has been published and can be found in [44,45]; these authors also report the model validation against several reference flows.

2.6. Cavitation Model Assessment

The cavitation model adopted for the current investigation and the related settings have been assessed simulating two reference cases, i.e., the experiment proposed by Winklhofer et al. [46] and the more recent experiment proposed by Sou et al. [47]. As recently reported in [19], many other contributors [48,49] have considered the experiment of Winklhofer as a significant reference case. This experiment is based on the investigation of an optically accessible channel (inlet section 0.300 × 0.301 mm; outlet section 0.284 × 0.301 mm; 1 mm length, 0.02 mm inlet curvature radius).

During the experimental research, the inlet pressure was fixed (10 MPa), at a uniform fuel temperature of 300 K, whereas the outlet pressure was adjusted in order to obtain the required flow rate. The same technique has been applied in the simulations. Figure 6 (left) shows the computational grid used in the cavitation model assessment; it represents 1/4th of the real channel geometry, thanks to symmetry of domain. The flow behavior of the throttle has been positively tested in several operating points. On one side, the hydraulic prediction has been found to be good agreement with experiments, as visible in Figure 6 (right) and in Table 2, which reports the details of mass flow rate in the conditions evidenced by [46] (cavitation incipience—Point A, critical cavitation—Point B and super cavitation—Point C). On the other side, the cavitation patterns related to the three fundamental conditions, as evidenced in [46], have been consistently reproduced, as reported in Figure 7; it has to be explicitly mentioned that the cavitation patterns observed by Winklhofer were fluctuating, due to the highly turbulent flow environment and they have been obtained by an ensemble averaging process of a set of twenty images taken under the same operating conditions.

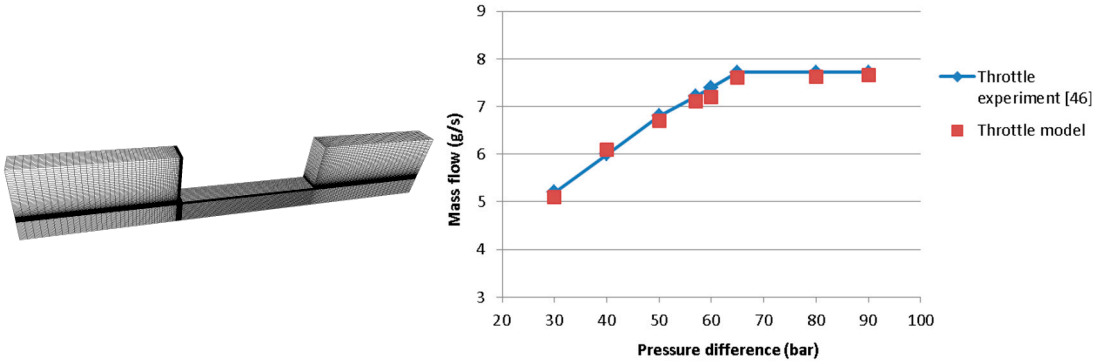

Figure 6. Computational grid used to model the experiment of Winklhofer et al. [46] (**left**); mass flow within the throttle channel (**right**).

Table 2. Mass flow conditions in throttle channel.

Conditions	Cavitation Start (A)		Critical Cavitation (B)		Super Cavitation (C)	
	Experiment	Model	Experiment	Model	Experiment	Model
Pressure difference (bar)	57.0	57.0	65.0	65.0	80	80
Mass flow (g/s)	7.21	7.1	7.72	7.60	7.72	7.63

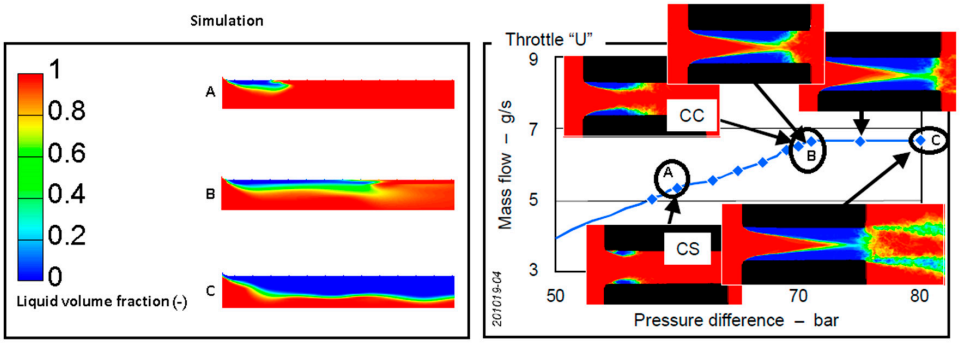

Figure 7. Cavitation at throttle flow conditions (**A**, **B**, **C**); simulated cavitation regions (**left**); experiment of Winklhofer et al. [46] (**right**); CS: cavitation start; CC: critical cavitation.

Moving to the second assessment phase, the experiment of Sou [47] has been reproduced by simulation. The experiment consists of a flow through a transparent channel allowing the visualization

(based on Laser Doppler Velocimetry) of cavitation incipience and development. In the experiments, a water flow is produced. The discharge ambient is kept at a constant pressure (ambient pressure) and the inflow condition is varied to realize different flow regimes, represented by the mean liquid velocity (V_n) in the channel. The incipience and the development of cavitation is well reproduced by the simulation, as indicated by the contours of liquid mass fraction shown in Figure 8. The quantitative comparison between the experiment and the simulation is reported in Figure 9, where the available data on velocity profile provided by Sou [47] are compared with the simulations. The trends are referred to three different axial locations along the throttle axis, as evidenced by the sketch of throttle layout of Figure 9. Good agreement has been found in all of the cases.

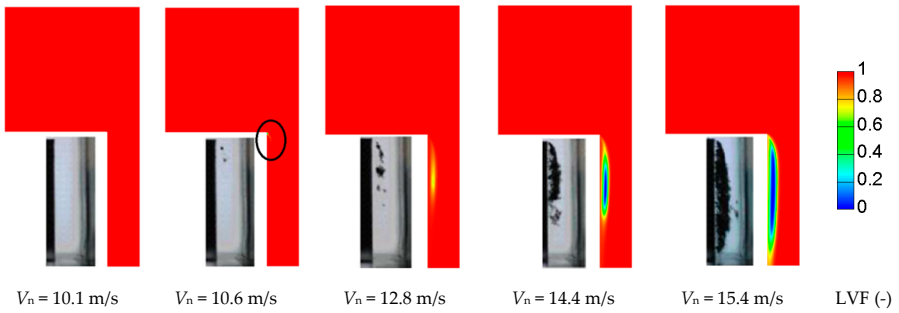

Figure 8. Cavitation at throttle flow conditions; simulation LVF (-) (liquid volume fraction) (**right**); Experiment of Sou et al. [47] (**left**), cavitation inception at black circle.

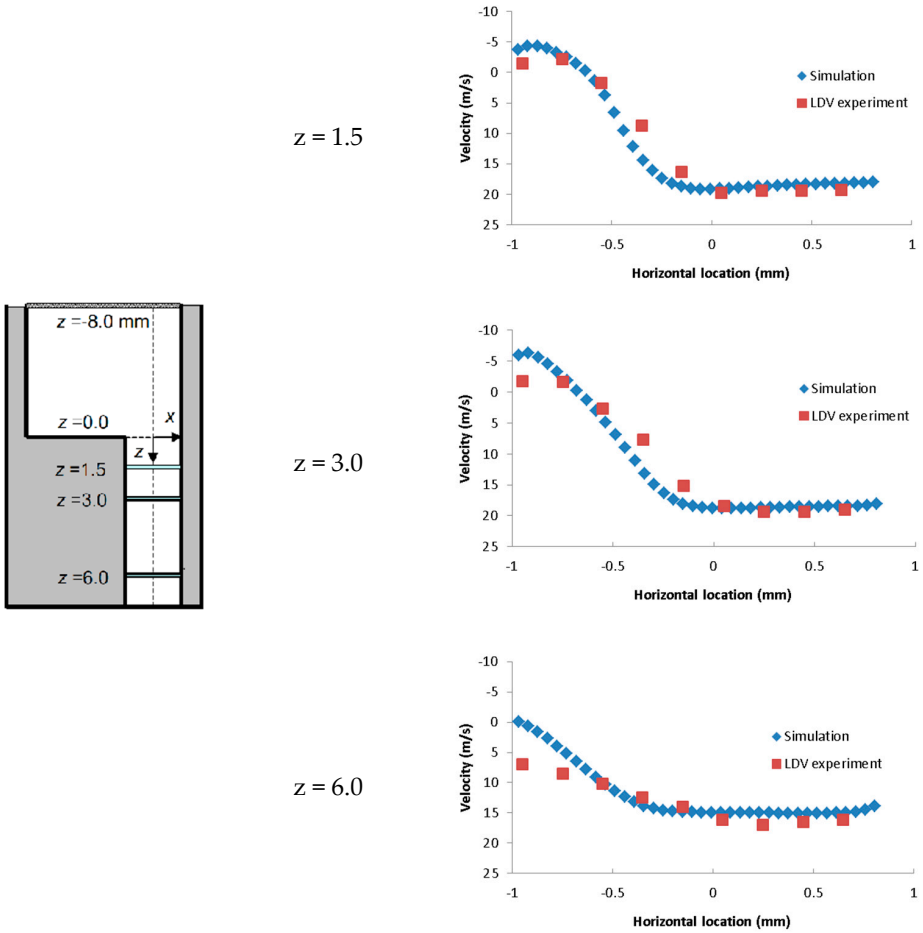

Figure 9. Velocity profiles in the nozzles at V_n = 12.8 m/s [47].

2.7. Grid Sensitivity Tests and Spray Model Assessment

Once the cavitation model is validated, a thorough pre-computation procedure has been performed to find the best computation settings on the used grids; the effect of local refinements has been evaluated as well. The tested grid types and the adopted cell number are listed in Table 3. In the same table, the mass flow rate differences among the nozzle flow tests are reported. Figure 10 reports the graphical results in terms of the velocity profile and cavitation development, when adopted, and the most refined nozzle grids are compared.

Table 3. Grid properties and adopted refinements.

Injector Nozzle			
mesh type Hexahedral-structured	min cell number 195,500	max cell number 3,800,000	adopted cell number 490,000
Mass flow rate % difference during refinement tests	7.4% more	1.6% less	reference case
Near nozzle region			
mesh type Hexahedral-structured	min cell number 11,760	max cell number 687,000	adopted cell number 94,080
Spray volume			
mesh type Hexahedral-structured	min cell number 54,230	max cell number 372,000	adopted cell number 105,984

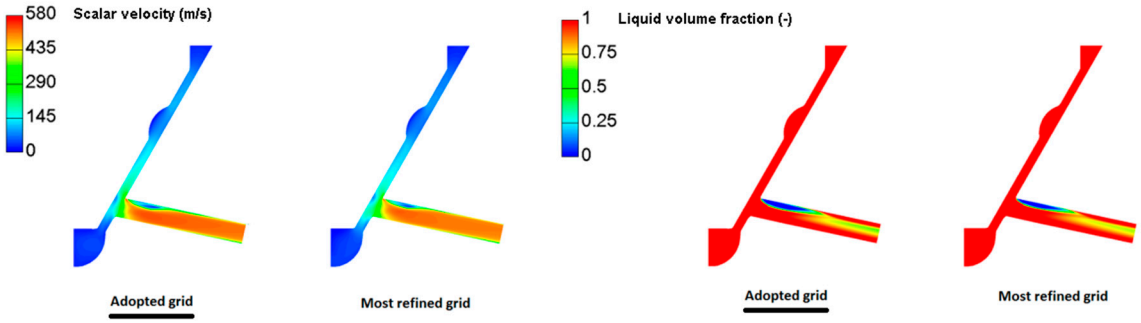

Figure 10. Velocity field contours and cavitation patterns in the case of the adopted and finest nozzle grid.

Since the spray model is used to chase the hole-to-hole spray differences, a crucial check in the current investigation is to assess the penetration dependence on computational grid refinement. Figure 11 (left) reports the trends obtained for the hole *N*1, depending on the refinement of spray domains.

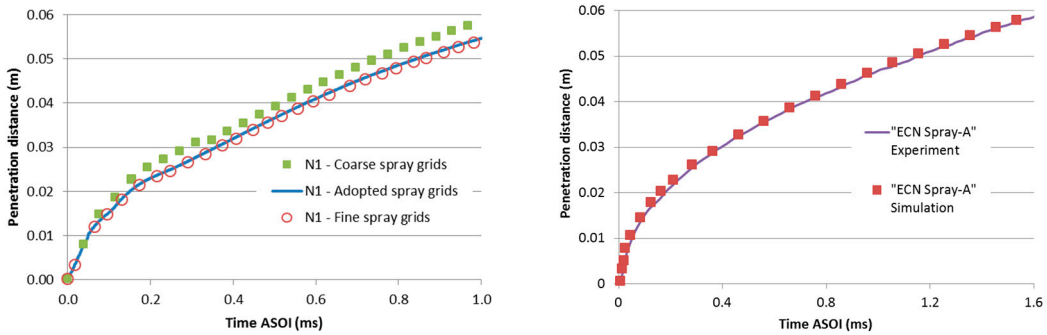

Figure 11. Penetration dependence on spray-domain refinement (**left**); spray model assessment against "ECN Spray-A" reference case (**right**).

The spray model capability has also been assessed against experimental data; Figure 11 (right) reports the comparison between experimental and simulated penetration lengths, referring to "ECN Spray-A" case [50], Table 4.

Table 4. Spray-A conditions.

Rail Pressure (MPa)	Ambient Pressure (MPa)	Ambient Temperature (K)	Nozzle Number	Fluid
150	6	900	210677	N-C12-H26

2.8. Non-Dimensional Coefficients

To allow the comparison among the holes, the results of the nozzle CFD model have been lumped in non-dimensional parameters that qualify the flow at each outlet section [45]. In the adopted scheme, Equation (16), the liquid-phase mass flow rate (m_r) passes through an effective area (A_e) with a uniform velocity (v_e); thus, vena contracta and cavitation affect the flow reducing the geometrical area (A_g) to the effective one (A_e). Considering an ideal flow, the theoretical velocity v_t, Equation (17), is defined by means of a Bernoulli equation, assuming negligible velocity at the inlet section. The theoretical mass flow passing through the geometrical nozzle outlet section (A_g) is given by Equation (18). The first non-dimensional parameter is the discharge coefficient, C_D defined as follows (Equation (19)):

$$m_r = \rho_l A_e v_e, \tag{16}$$

$$v_t = \sqrt{\frac{2(P_{inj} - P_{back})}{\rho_l}}, \tag{17}$$

$$m_t = \rho_l A_g v_t, \tag{18}$$

$$C_D = \frac{m_r}{m_t}. \tag{19}$$

In order to isolate the area from the velocity contribute, the discharge coefficient is viewed as the product of two further non-dimensional parameters C_V and C_A, Equation (20):

$$C_D = C_A . C_V, \tag{20}$$

$$C_V = \frac{v_{eff}}{v_t}, \tag{21}$$

$$C_A = \frac{A_{eff}}{A_g}. \tag{22}$$

3. Results

3.1. Hole-to-Hole Difference on Spray Penetration

As a first step in analyzing the results, it has been checked whether the off-axis of the needle is tied to significant differences on the spray; accordingly, the penetration trends over time for each nozzle hole have been observed. The penetration distance is defined as the distance along the spray axis to the boundary of the spray, according to [51]. The curves of Figure 6 originate at time zero ASOI (After Start Of Injection) and reach the penetration of 0.01 m at different times. Incidentally, up to 0.01 m, the spray is in the Eulerian–Eulerian domain; when droplets exceed this limit, they are taken over by the Eulerian–Lagrangian simulation. The spray emerging from the hole *N*2 is the slowest, both in the Eulerian tract for the half part of the Lagrangian tract. Referring to the off-axis configuration of Figure 3, the comparisons were made in couples, first *N*4 and *N*1, then *N*2 and *N*3 and finally the pair *N*1–*N*3; the related trends, in terms of percentage differences, are shown in Figure 12 (right).

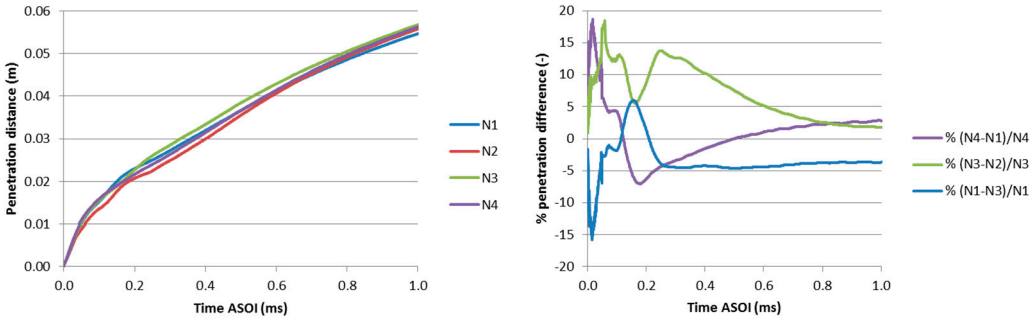

Figure 12. Spray penetration of simulated sprays (**left**); % penetration difference among the sprays (**right**).

Since the opening of the nozzle up to 0.1 ms ASOI, spray *N*4 prevails over spray N1; this difference decreases rapidly, vanishes in 0.11 ms ASOI and reverses back, up to more than half of the injection process. In the closing phase, the spray N4 returns to prevail on the spray N1 but with a more limited deviation to what occurs at the opening (3% versus 18%).

During the opening, the pair *N*3–*N*2 behaves likewise to the pair *N*4–*N*1, with the prevalence of *N*3 on *N*2, but, thereafter, the difference, while decreasing, does not fade and 0 is not reversed.

The trend of the pair *N*1–*N*3 shows the spray *N*1 below *N*3, but not in the period between 0.11 and 0.2 ms ASOI.

A graphical evolution of the spray shape, accompanied by the cut view of the nozzle flow, is reported in Figure 13; even if the thorough analysis of the flow structures within the nozzle is beyond the aim of the current contribution, it is desirable to focus on how the penetration dispersion among the holes is reflected by the shape of the spray plumes; the asymmetry of velocity and cavitation patterns is clearly evident.

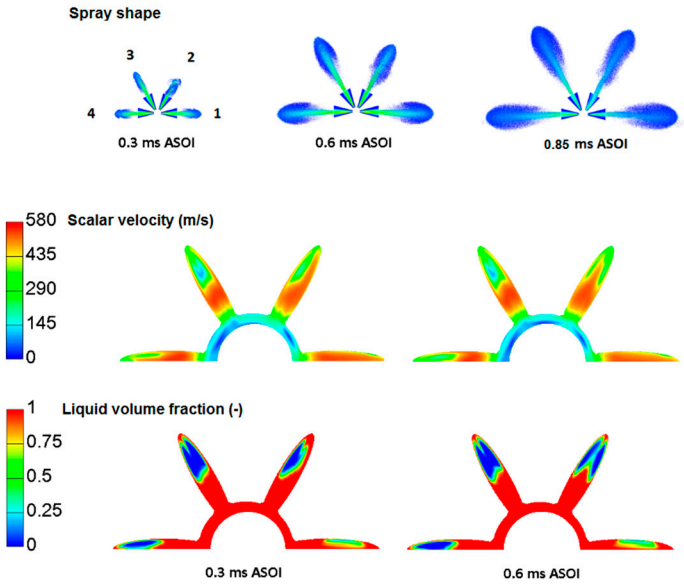

Figure 13. Shape of the four sprays (numbered according to Figure 3) and cut views of the internal nozzle flow.

3.2. Hole-to-Hole Differences for Spray Sauter Mean Diameter (SMD)

Time trends of the global SMD (Sauter Mean Diameter) for different sprays are shown in Figure 14, while maintaining the same comparison method based on couples seen in the previous paragraph.

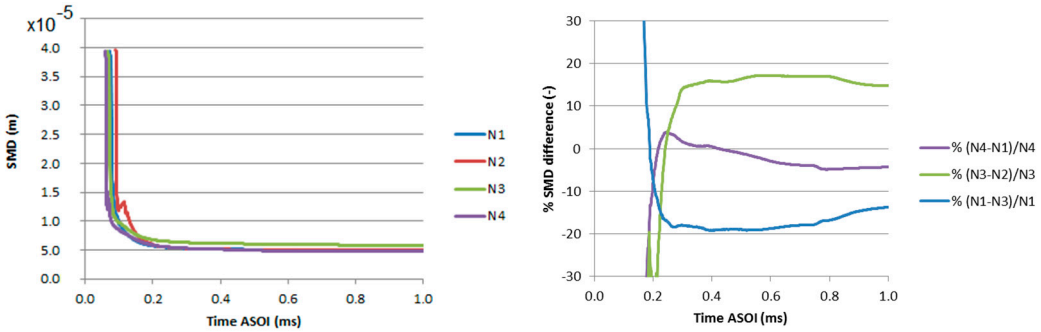

Figure 14. SMD (Sauter Mean Diameter) of the spray versus time (**left**); % difference on SMD among the sprays (**right**).

With reference to the pair *N*4–*N*1, from the opening up to 0.21 ms ASOI, spray *N*1 shows significantly higher SMD values. The behavior is reversed for a short period, up to 0.42 ms ASOI, after which the spray *N*4 returns to exhibit lower SMD, with percentage differences within 5%.

The trend of the pair *N*3–*N*2 sees much lower initial values for the spray *N*3, but the behavior is reversed in 0.24 ms ASOI. The SMD of spray *N*2 assumes the values of the other cases throughout the rest of the injection, about 15% below *N*3.

The pair *N*1–*N*3 still highlights the high SMD value of *N*3, which exceeds *N*1 as low as 0.21 ms ASOI with differences very close to 20%.

3.3. Flow Features at the Outlet of the Holes

In the interpretation of the spray behavior seen previously, the trends of discharge-coefficient C_D, velocity-coefficient C_V and area-coefficient C_A have been obtained for each hole, based on the 3D-CFD nozzle flow modeling. Maximum value of C_D is encountered when the needle is at maximum lift, and it is limited slightly below 0.3. According to [6], such a value could be expected for the same conditions in terms of pressure but at lower needle lift. Here, the obtained value reflects the geometrical features of the considered nozzle; indeed, the configuration of the needle closing passage in the modeled nozzle is able to influence the flow even at relatively high lift values, affecting the flow rate significantly.

Up to 0.2 ms ASOI, the hole *N*2 is characterized by the lesser fuel delivery, Figure 15. In this time interval, the flow rate is penalized by both coefficients C_V and C_A, shown in the graphs in Figure 16. This indicates that, in the initial stages of injection, the fluid reaches the output section of hole *N*2 with relatively low velocity and that the section of the hole is moderately active. The trends of Figure 13 reflect this scenario; the intensity of cavitation at the outlet section is relatively moderate (the liquid volume fraction is relatively high) in addition to the turbulence kinetic energy. In this initial period of the injection process, the mass flow rate is affected by an evident irregularity, which is slightly reproduced in the closing phase of injection. Such a behavior is in agreement with what was found in [17], and it is typically due to the flow perturbations induced by the needle eccentricity.

After 0.2 ms ASOI, the behavior of hole *N*2 changes. The trend of discharge coefficient C_D is modified and from 0.4 ms ASOI becomes similar to that of *N*1 and *N*4 cases. The trend of the liquid fraction is similar to those of the other holes, except in the closing phase, where an increase is visible, accompanied by similar deviations of turbulence kinetic energy and C_A coefficient.

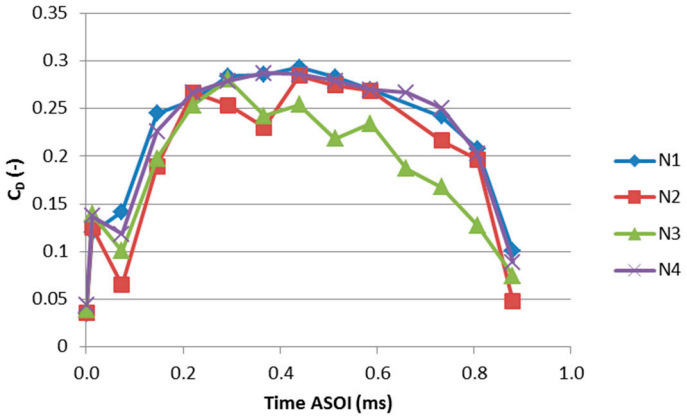

Figure 15. Nozzle hole discharge coefficient Cd and mass flow of injected liquid phase.

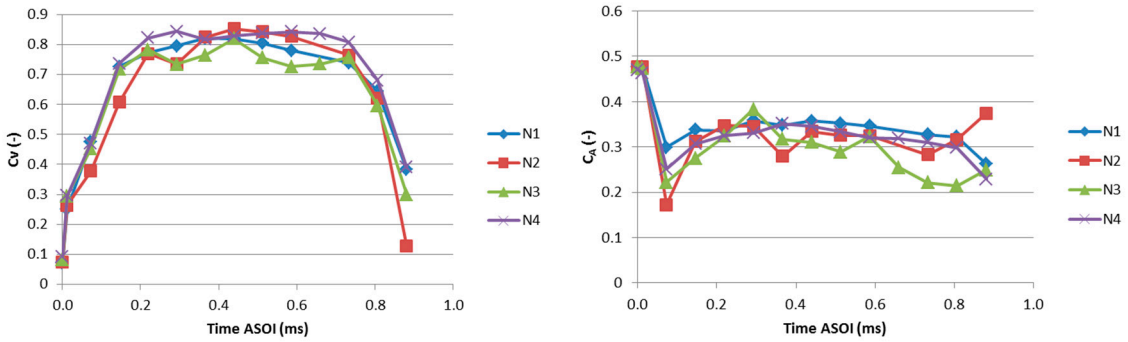

Figure 16. Nozzle hole velocity coefficient C_V (**left**), nozzle hole Area coefficient C_A (**right**).

The discharge coefficient C_D of hole *N*3 is relatively high during the initial stage of the injection, in contrast to what was seen in the *N*2 case. The velocity coefficient C_V is aligned to the values of the other cases and the area coefficient C_A indicates a relatively good utilization of the hole area. The liquid fraction reaches the lowest value at about 0.1 ms ASOI (Figure 17), and the trend of turbulence kinetic energy is relatively high with downward concavity. This scenario changes at 0.3 ms ASOI. The discharge coefficient C_D starts decreasing significantly (Figure 15), due to the drop of C_V and C_A (Figure 16).

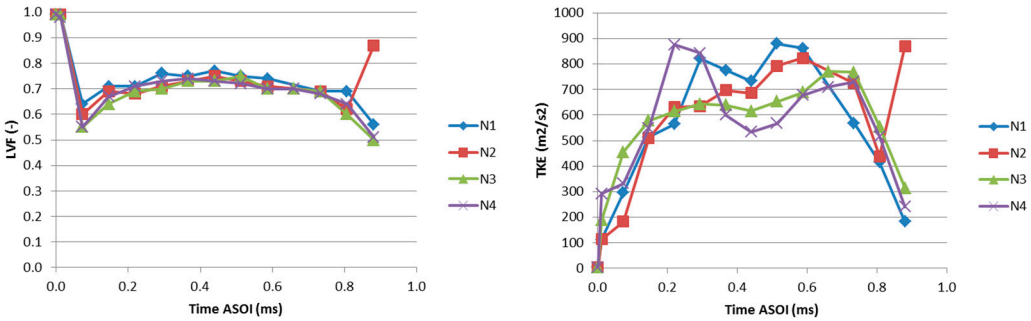

Figure 17. Liquid volume fraction at nozzle hole outlet section (-) (**left**); turbulent kinetic energy at nozzle hole outlet section (m^2/s^2) (**right**).

The *N*1 and *N*4 holes show slight differences in mass flow rate (Figure 15) and the needle off-axis effects are better highlighted by the trends of coefficients C_A and C_V (Figure 16). The coefficients indicate that the outlet velocity at hole *N*4 is higher; this factor does not significantly increase the mass

flow since it is balanced by the reduced utilization of the geometric section of the hole, due to stronger cavitation. Indeed, the trends of Figure 17 show the lower liquid fraction at the exit section of hole *N*4, compared to the case *N*1.

4. Conclusions

The current study showed that the lack of homogeneity in the mass-flow distribution is certainly a key factor behind the spray irregularities, but also that it is not the only one. In fact, even when the same discharge coefficient is found among the holes, irregularities are observed among the far sprays. The irregularities have been evidenced by the dispersion of penetration among the different orifices, and they have been addressed to the nozzle configuration by analyzing the flow features in terms of non-dimensional parameters. The velocity-coefficient C_V and the area-coefficient C_A have been found to provide valuable information to completely represent the flow conditions at nozzle outlets when needle off-axis is encountered.

The 3D-CFD modeling retains major relevance in the determination of these coefficients, due to the difficulties that would arise by the experimental techniques. In this scenario, the coupling with the spray models is the crucial step to quantify the differences that cannot be assessed only through the analysis of mass flow rate distribution.

From the industrial viewpoint, the current study made it possible to identify the range of variability that can be expected from the VCO nozzles, in the typical operating conditions of common rail systems (ballistic needle displacement and reduced lift), and the range of variability within the spray characteristics, expected to vary, has been defined. In the current case, these ranges have been found on the order of 15% for penetration and in the order of 20% for global SMD; following the same approach, these ranges can be identified for other specific injectors and operating conditions.

The values of C_V and C_A coefficients can be taken as a reference in further investigations (three-dimensional, multi-zone, or lumped-parameter based), in order to explore the effects of spray non-idealities on the engine performance, on the combustion behavior and, more generally, on those cases affected by sensitivity to the spray characteristics.

Acknowledgments: The authors acknowledge the fundamental contribution of AVL List–Graz providing the *FIRE*™ code and giving the necessary support during the research activities.

Author Contributions: Giancarlo Chiatti conceived and organized the work; Ornella Chiavola and Fulvio Palmieri designed the investigations, analyzed the data and wrote the article; Pierluigi Frezzolini performed numerical simulations.

Conflicts of Interest: The authors declare no conflict of interest.

Nomenclature

Roman	*Description (Unit)*
k,l	Eulerian class index
∇p	pressure gradient (Pa/m)
$\boldsymbol{f}$	body force vector (N/m^3)
h	specific enthalpy (J/kg)
$M_{k,l}$	momentum exchange term between phase k and l (N/m^3)
$H_{k,l}$	heat flux vector (W/m^2)
t	time (s)
dt	calculation time step
WF	weighting factor
v	velocity vector (m/s)
Greek	*Description (Unit)*
α	volume fraction (–)

θ	enthalpy volumetric source (W/kg)
ρ	density (kg/m^3)
τ	shear stress tensor (N/m^2)
$\Gamma_{k,l}$	mass exchange term between phase *k* and *l* (kg/(m^3 s))
ε	turbulence dissipation rate (m^2/s^3)
Subscripts	*Description*
k	phase index
ex	extensive property
in	intensive property
NN	near nozzle
SV	spray volume
Superscripts	*Description*
t	turbulent index
Abbreviations	*Description*
ASOI	after start of injection
3D-CFD	three-dimensional computational fluid dynamics
CV	control volume
DDM	discrete droplet method
RANS	Reynolds-averaged Navier-Stokes
SMD	Sauter mean diameter
VCO	valve covered orifice
LVF	liquid volume fraction

References

1. Stan, C. *Direct Injection Systems for Spark-Ignition and Compression-Ignition Engines*; Society of Automotive Engineers (SAE): Troy, MI, USA, 2000.
2. Eagle, W.E.; Musculus, M.P.B. Cinema-Stereo Imaging of Fuel Dribble after the End of Injection in an Optical Heavy-Duty Diesel Engine. In Proceedings of the Thiesel Conference on Thermo and Fluid Dynamic Processes in Direct Injection Engines, Valencia, Spain, 9–12 September 2014.
3. Crua, C.; Heikal, M.R.; Gold, M.R. Microscopic imaging of the initial stage of diesel spray formation. *Fuel* **2015**, *157*, 140–150. [CrossRef]
4. Ghiji, M.; Goldsworthy, L.; Brandner, P.A.; Garaniya, V.; Hield, P. Analysis of diesel spray dynamics using a compressible Eulerian/VOF/LES model and microscopic shadowgraphy. *Fuel* **2017**, *188*, 352–366. [CrossRef]
5. Papadopoulos, N.; Aleiferis, P. Numerical Modelling of the in-Nozzle Flow of a Diesel Injector with Moving Needle during and after the End of a Full Injection Event. *SAE Int. J. Eng.* **2015**, *8*, 2285–2302. [CrossRef]
6. Bermúdez, V.; Payri, R.; Salvador, F.J.; Plazas, A.H. Study of the influence of nozzle seat type on injection rate and spray behavior. *Proc. Inst. Mech. Eng. Part D J. Automob. Eng.* **2005**, *219*, 677–689.
7. Salvador, F.J.; Carreres, M.; Jaramillo, D.; Martínez-López, J. Comparison of microsac and VCO diesel injector nozzles in terms of internal nozzle flow characteristics. *Energy Convers. Manag.* **2015**, *103*, 284–299. [CrossRef]
8. Moro, A.; Zhou, Q.; Xue, F.; Luo, F. Comparative study of flow characteristics within asymmetric multi hole VCO and SAC nozzles. *Energy Convers. Manag.* **2017**, *132*, 482–493. [CrossRef]
9. Chiatti, G.; Chiavola, O.; Recco, E.; Palmieri, F. Soot Particles Experimental Characterization during Cold Start of a Micro Car Engine. *Energy Proced.* **2016**, *101*, 662–669. [CrossRef]
10. Eagle, W.E.; Musculus, M.P.B. Image-Based Correlation of Engine Operating Parameters with Occurrence and Duration of Diesel Fuel Injector Dribble. In Proceedings of the Oral Communication at SAE World Congress 2015, Detroit, MI, USA, 21–23 April 2015.
11. Mitroglou, N.; Gavaises, M.; Arcoumanis, D. *Spray Stability from VCO and a New Diesel Nozzle Design Concept*; Fuel Systems for IC Engines; IMechE: London, UK, 2012.
12. Chiatti, G.; Chiavola, O.; Palmieri, F. Diesel Nozzle Flow Investigation in Non-Radial Multi Hole Geometry, ASME Paper 5556. In Proceedings of the 2014 Internal Combustion Engine Division Fall Technical Conference, Columbus, IN, USA, 19–22 October 2014.
13. Bae, C.; Kang, J. Diesel Spray Development of VCO Nozzles for High Pressure Direct-Injection. *SAE Tech. Pap.* **2000**. [CrossRef]

14. De Risi, A.; Colangelo, G.; Laforgia, D. An Experimental Study of High-Pressure Nozzles in Consideration of Hole-To-Hole Spray Abnormalities. *SAE Tech. Pap.* **2000**. [CrossRef]
15. Oda, T.; Hiratsuka, M.; Goda, Y.; Kanaike, S.; Ohsawa, K. Experimental and Numerical Investigation about Internal Cavitating Flow and Primary Atomization of a Large-scaled VCO Diesel Injector with Eccentric Needle. In Proceedings of the ILASS-Europe, Brno, Czech Republic, 6–9 September 2010.
16. Fezzaa, K.; Lee, W.K.; Cheong, S.; Powell, C.F.; Wang, J.; Li, M.; Lai, M.C. *High Pressure Diesel Injection Studied by Time-Resolved X-ray Phase Contrast Imaging*; ICES2006 ASME: New York, NY, USA, 2006.
17. Battistoni, M.; Xue, Q.; Som, S.; Pomraning, E. Effect of Off-Axis Needle Motion on Internal Nozzle and Near Exit Flow in a Multi-Hole Diesel Injector. *SAE Int. J. Fuels Lubr.* **2014**, *7*, 167–182. [CrossRef]
18. Palmieri, F. The Influence of Actual Layout and Off-Axis Needle Stroke on Diesel Nozzle Flow under Ballistic Needle Displacement. *J. Eng. Gas Turbines Power* **2013**, *135*, 101502. [CrossRef]
19. Xue, F.; Luo, F.; Cui, H.; Moro, A.; Zhou, L. Numerical analyses of transient flow characteristics within each nozzle hole of an asymmetric diesel injector. *Int. J. Heat Mass Transf.* **2017**, *104*, 18–27. [CrossRef]
20. Salvador, F.J.; Martínez-López, J.; Romero, J.-V.; Roselló, M.-D. Study of the influence of the needle eccentricity on the internal flow in diesel injector nozzles by computational fluid dynamics calculations. *Int. J. Comput. Math.* **2014**, *91*, 24–31. [CrossRef]
21. Xue, Q.; Battistoni, M.; Powell, C.F.; Longman, D.E.; Quan, S.P.; Pomraning, E.; Senecal, P.K.; Schmidt, D.P.; Som, S. An Eulerian CFD model and X-ray radiography for coupled nozzle flow and spray in internal combustion engines. *Int. J. Multiph. Flow* **2015**, *70*, 77–88. [CrossRef]
22. Payri, R.; Viera, J.P.; Gopalakrishnan, V.; Szymkowicz, P.G. The effect of nozzle geometry over the evaporative spray formation for three different fuels. *Fuel* **2017**, *188*, 645–660. [CrossRef]
23. Petranović, Z.; Edelbauer, W.; Vujanović, M.; Duić, N. Modelling of spray and combustion processes by using the Eulerian multiphase approach and detailed chemical kinetics. *Fuel* **2017**, *191*, 25–35. [CrossRef]
24. FIRE Rev.14.2. *User's Guide, Solver Manual. Eulerian Multiphase Manual, Spray Manual*; AVL List: Graz, Austria, 2016.
25. LMS Imagine. Lab. AMESim Manuals. In *Technical Bulletins and Libraries*; Release 14; Steris Life Sciences: Mentor, OH, USA, 2014.
26. Bosch, W. The Fuel Rate Indicator: A New Measuring Instrument for Display of the Characteristics of Individual Injection. *SAE Tech. Pap.* **1966**. [CrossRef]
27. Marini, J. Studio e Modellazione del Comportamento Meccanico-Idraulico di Polverizzatori di Elettroiniettori Diesel Common-Rail. Master's Thesis, Roma TRE University, Rome, Italy, 2016.
28. Manin, J.; Kastengren, A.; Payri, R. Understanding the acoustic oscillations observed in the injection rate of a common-rail direct injection diesel injector. *J. Energy Power Eng.* **2012**, *134*, 122801. [CrossRef]
29. Desantes, J.M.; García-Oliver, J.M.; Pastor, J.M.; Pandal, A.; Baldwin, E.; Schmidt, D.P. Coupled/decoupled spray simulation comparison of the ECN spray a condition with the σ-Y Eulerian atomization model. *Int. J. Multiph. Flow* **2016**, *80*, 89–99. [CrossRef]
30. Pandal, A.; Pastor, J.M.; García-Oliver, J.M.; Baldwin, E.; Schmidt, D.P. A consistent, scalable model for Eulerian spray modeling. *Int. J. Multiph. Flow* **2016**, *83*, 162–171. [CrossRef]
31. Vallet, A.; Burluka, A.A.; Borghi, R. Development of an Eulerian model for the "atomization" of a liquid jet. *At. Sprays* **2001**, *11*, 619–642. [CrossRef]
32. Blokkeel, G.; Barbeau, B.; Borghi, R. A 3D Eulerian model to improve the primary breakup of atomizing jet. *SAE* **2003**. [CrossRef]
33. Demoulin, F.X. Coupling vaporization model with the Eulerian–Lagrangian Spray Atomization (ELSA) model in diesel engine conditions. *SAE Tech. Pap.* **2005**. [CrossRef]
34. Ning, W.; Reitz, R.D.; Diwakar, R.; Lippert, A.M. An Eulerian–Lagrangian spray and atomization model with improved turbulence modeling. *At. Sprays* **2009**, *19*, 727–739. [CrossRef]
35. Hoyas, S.; Gil, A.; Margot, X.; Khuong-Anh, D.; Ravet, F. Evaluation of the Eulerian–Lagrangian Spray Atomization (ELSA) model in spray simulations: 2D cases. *Math. Comput. Model.* **2013**, *57*, 1686–1693. [CrossRef]
36. Krueger, C. Validation of a 1D spray model for simulation of mixture formation in direct injection Diesel engines. Ph.D. Thesis, RWTH Aachen, Aachen, Germany, 2001.

37. Edelbauer, W.; Suzzi, D.; Sampl, P.; Tatschl, R.; Krueger, C.; Weigand, B. New concept for on-line coupling of 3D Eulerian and Lagrangian spray approaches in engine simulations. In Proceedings of the 10th International Conference on Liquid Atomisation and Spray Systems, Kyoto, Japan, 27 August–1 September 2006.
38. Edelbauer, W. Coupling of 3D Eulerian and Lagrangian spray approaches in industrial combustion engine simulations. *J. Energy Power Eng.* **2014**, *8*, 190–200.
39. Vujanović, M.; Petranović, Z.; Edelbauer, W.; Duić, N. Modelling spray and combustion processes in diesel engine by using the coupled Eulerian–Eulerian and Eulerian–Lagrangian method. *Energy Convers. Manag.* **2016**, *125*, 15–25. [CrossRef]
40. Drew, D.A.; Passman, S.L. *Theory of Multicomponent Fluids*; Springer: Berlin, Germany, 1998.
41. Patterson, M.A.; Reitz, R.D. Modeling the Effects of Fuel Spray Characteristics on Diesel Engine Combustion and Emissions. *SAE Tech. Pap.* **1998**. [CrossRef]
42. O'Rourke, P.J.; Bracco, F.V. *Modelling of Drop Interactions in Thick Sprays and a Comparison with Experiments*; IMechE: London, UK, 1980.
43. Sato, Y.; Sekoguchi, K. Liquid Velocity Distribution in Two-Phase Bubble Flow. *Int. J. Multiph. Flow* **1975**, *2*, 79–95. [CrossRef]
44. Wang, D.M.; Greif, D. Progress in modeling injector cavitating flows with a multi-fluid method. In Proceedings of the ASME 2006 2nd Joint US-European Fluids Engineering Summer Meeting Collocated with the 14th International Conference on Nuclear Engineering, Miami, FL, USA, 17–20 July 2006; American Society of Mechanical Engineers: New York, NY, USA, 2006; pp. 153–162.
45. Von Berg, E.; Edelbauer, W.; Alajbegovic, A.; Tatschl, R.; Volmajer, M.; Kegl, B.; Ganippa, L.C. Coupled simulations of nozzle flow, primary fuel jet breakup, and spray formation. *J. Eng. Gas Turbines Power* **2005**, *127*, 897–908. [CrossRef]
46. Winklhofer, E.; Kull, E.; Kelz, E.; Morozov, A. Comprehensive hydraulic and flow field documentation in model throttle experiments under cavitation conditions. In Proceedings of the ILASS-Europe Conference, Zurich, Switzerland, 2–6 September 2001; pp. 574–579.
47. Sou, A.; Biçer, B.; Tomiyama, A. Numerical simulation of incipient cavitation flow in a nozzle of fuel injector. *Comput. Fluids* **2014**, *103*, 42–48. [CrossRef]
48. Salvador, F.J.; Romero, J.V.; Roselló, M.D.; Martínez-López, J. Validation of a code for modeling cavitation phenomena in Diesel injector nozzles. *Math. Comput. Model.* **2010**, *52*, 1123–1132. [CrossRef]
49. Som, S.; Aggarwal, S.K.; El-Hannouny, E.M.; Longman, D.E. Investigation of nozzle flow and cavitation characteristics in a diesel injector. *J. Eng. Gas Turbines Power* **2010**, *132*, 042802. [CrossRef]
50. Spray-A Characterization Data, Engine Combustion Network. Available online: https://ecn.sandia.gov/ecn-data-search/ (accessed on 1 January 2017).
51. Naber, J.; Siebers, D. Effects of Gas Density and Vaporization on Penetration and Dispersion of Diesel Sprays. *SAE Tech. Pap.* **1996**. [CrossRef]